AN ABSTRACT OF THE THESIS OF

Scott Heffernan for the degree of Master of Science in Sustainable Forest Management presented on September 5, 2018.

Title: Estimation of surface canopy water in Pacific Northwest forests by fusing radar, lidar, and climatic data.

Abstract approved: _____

Bogdan M Strimbu

Surface Canopy Water (SCW) is the intercepted rain water that resides within the tree canopy and plays a significant role in the hydrological cycle. Challenges arise in measuring SCW in remote areas using traditional ground based techniques. Remote sensing in the radio spectrum has the potential to overcome the challenges where traditional modelling approaches face difficulties. In this study we investigated the capability of the most recent SAR platform, the Sentinel-1 constellation to estimate SCW. We measured the backscatter of six forest stands in the H J Andrews experimental forest in central Oregon (as well as four clear cut areas and one golf course) over three summers to describe how the backscatter signal changes with moisture. We found significant results when we executed the analysis on radar images on which individual trees crowns were delineated from lidar, as opposing to SCW estimated from individual pixels backscatter. Significant differences occur in the mean backscatter between radar images taken during rain vs. during dry periods (no rain for > 1h). A lack in sufficient data prevented the formulation of a robust predictive model, however our results suggest the posibilty of mapping canopy moisture using SAR in the Pacific Northwest.

Estimation of surface canopy water in Pacific Northwest forests by fusing radar, lidar, and climatic data

by
Scott Heffernan

A THESIS

submitted to

Oregon State University

in partial fulfillment of
the requirements for the
degree of

Master of Science

Presented September 5, 2018
Commencement June 2019

Master of Science thesis of Scott Heffernan presented on September 5, 2018

APPROVED:

Major Professor, representing Sustainable Forest Management

Head of the Department of Forest Engineering, Resources, and Management

Dean of the Graduate School

I understand that my thesis will become part of the permanent collection of Oregon State University libraries. My signature below authorizes release of my thesis to any reader upon request.

Scott Heffernan, Author

ACKNOWLEDGEMENTS

I would like to thank my parents Michael and Tina Heffernan for inspiring and supporting my curiosity from an early age. I would also like to thank Dr. Bogdan Strimbu for being an incredible advisor and mentor.

Radar data were provided by the European Space Agency through the Copernicus Earth Observation program.

Weather data were provided by the HJ Andrews Experimental Forest and Long Term Ecological Research program, administered cooperatively by the USDA Forest Service Pacific Northwest Research Station, Oregon State University, and the Willamette National Forest. This material is based upon work supported by the National Science Foundation under Grant No. DEB-1440409

CONTRIBUTION OF AUTHORS

Scott Heffernan processed the data, executed the statistical analysis and wrote the thesis.

Dr. Strimbu assisted in statistical modelling and interpretation of the results.

TABLE OF CONTENTS

LIST OF FIGURES

Figure Page

LIST OF TABLES

Table Page

Estimation of surface canopy water in Pacific Northwest forests by fusing radar, lidar, and climatic data

1 Introduction

Surface canopy water (SCW), which is the intercepted rain water resting on the tree surfaces within the canopy layer, plays a significant role not only on the hydrological cycle but also on the characteristics of the boundary layer of the troposphere (De Ridder 2001) . To describe the atmospheric processes occurring above the forest, the amount of SCW existing at any moment in time is needed. The extensive networks of weather stations make the prediction of SCW relatively easy and accurate in relatively flat areas, but significant challenges are faced in mountainous or remote regions, as more complex extrapolations are required or crucial parameters may be unknown. Remotely sensed data can enhance prediction of SCW in areas where the traditional modelling approaches face difficulty. The critical aspect of using remote sensing data in any investigation is the selection of the appropriate wavelengths. Although the visible and near-infrared spectrum are used to measure the secondary effects of SCW on the color of the canopy, radio waves can directly measure the dielectric constant from water. Not only are radio waves suitable for water investigations, but in many situations radar (**RA**dio **D**irection **A**nd **R**anging) is preferred over passive optical sensors. This is because active microwave systems such as radar 1) are able to penetrate cloud cover and vegetation (although the penetration power depends highly on the wavelength), 2) are independent of local solar intensity, which allows operation irrespective day or night, and 3) are sensitive to surface roughness, moisture, and dielectric properties (Sinha et al. 2015). However, radar remote sensing presents several challenges, particularly 1) diversity of scattering processes, 2) coarse spatial resolution, and 3) lack of multiple bands (such as RGBI etc). Nevertheless, thanks to

the ability for all-weather measurements, forests under constant cloud cover, such as those in Pacific North West (PNW), can be investigated remotely.

Synthetic Aperture Radar (SAR) is the most common imaging radar. SAR uses the motion of the sensor's platform (typically a satellite or aircraft) and high precision and coordination of received signals to build a virtual aperture much larger than the actual antenna. Of the SAR sensors used in remote sensing, those working in the X, C, L, and P bands are the most informative of forest properties. The X-band, having a wavelength of about 3 cm, is informative of surface-level properties of the canopy because it is mainly scattered by the surface of the canopy. The C-band has a longer wavelength (~ 5.6 cm) and is able to penetrate into the canopy, although not necessarily the entire canopy (Van Zyl 1993). The C-band is mainly scattered by leaves and branches within the canopy during leaf-off conditions or some species with sparse canopies, such as Ponderosa pine. The L-band (wavelength 24 cm) and P-band (wavelength 30-60 cm) are mostly scattered by branches, trunks, and the ground. These longer wavelengths are informative of processes occurring below the canopy, such as surface inundation and woody biomass estimation. SAR can record data in different polarization states, which are HH (horizontally polarized transmitted pulse and horizontally polarized received signal), VV (vertical-vertical), and either VH or HV (horizontal transmit and vertical receive or vice-versa). The effects of vegetation on the scattering differs between polarization modes, as well as wavelength. For instance, it was found by (Le Toan et al. 1992) that for the L-band the cross-polarization modes (HV or VH) were suited for estimating biomass compared to the co-polarization modes (VV or HH). Mitchard et al. (2009) found that for the L-band the HH polarization is more susceptible to vegetation moisture than HV polarization.

1.1 Geometric Conventions of Radar

Radar can either be in slant range geometry or ground range geometry. Slant range geometry measures distance between the target and the antenna (Figure 1, A_β), whereas ground range measures distance between the ground track of the platform and the target (Figure 1 A_γ). Radar natively produces images in slant range, and ground range images require a transformation at each point in a radar image, and generally requires information on the terrain features (slope, elevation, aspect).

Radar backscatter geometry can be referenced in three different ways: *Beta-naught* (β^0), *Sigma-naught* (σ^0), and *Gamma-naught* (γ^0). Radar backscatter β is the ratio of scattered power P_a and incident power P_i, (Eq. 1):

$$\beta = \frac{P_a}{P_i} \quad 1$$

When operating in slant range geometry, the radar brightness is known as Beta-naught backscatter, which is the ratio between the backscatter and the area of illumination in the slant-range plane (Figure 1, A_β) :

$$\beta^0 = \frac{\beta}{A_\beta} \quad 2$$

If the reference area is defined as locally tangent to an ellipsoid model of the surface (the simple ground range geometry; Figure 1, A_σ) the brightness is known as Sigma-naught backscatter:

$$\sigma^0 = \beta^0 * \frac{A_\beta}{A_\sigma} = \beta^0 * sin\theta_E \quad 3$$

In addition, one can define the reference area as perpendicular to the line of sight, similar to how a photograph is to a camera (Figure 1, A_γ). In this case, Gamma-naught is the measure of backscatter:

$$\gamma^0 = \beta^0 * \frac{A_\beta}{A_\gamma} = \beta^0 * tan\theta_E \quad 4$$

In the case of σ^0 and γ^0 the variable θ_E is the local incidence angle on the ellipsoid. As described in (Small 2011), the β^0 and σ^0 conventions perform poorly in regions of topographic variation, and in the same paper describes the development of the γ^0 normalization convention used in this paper.

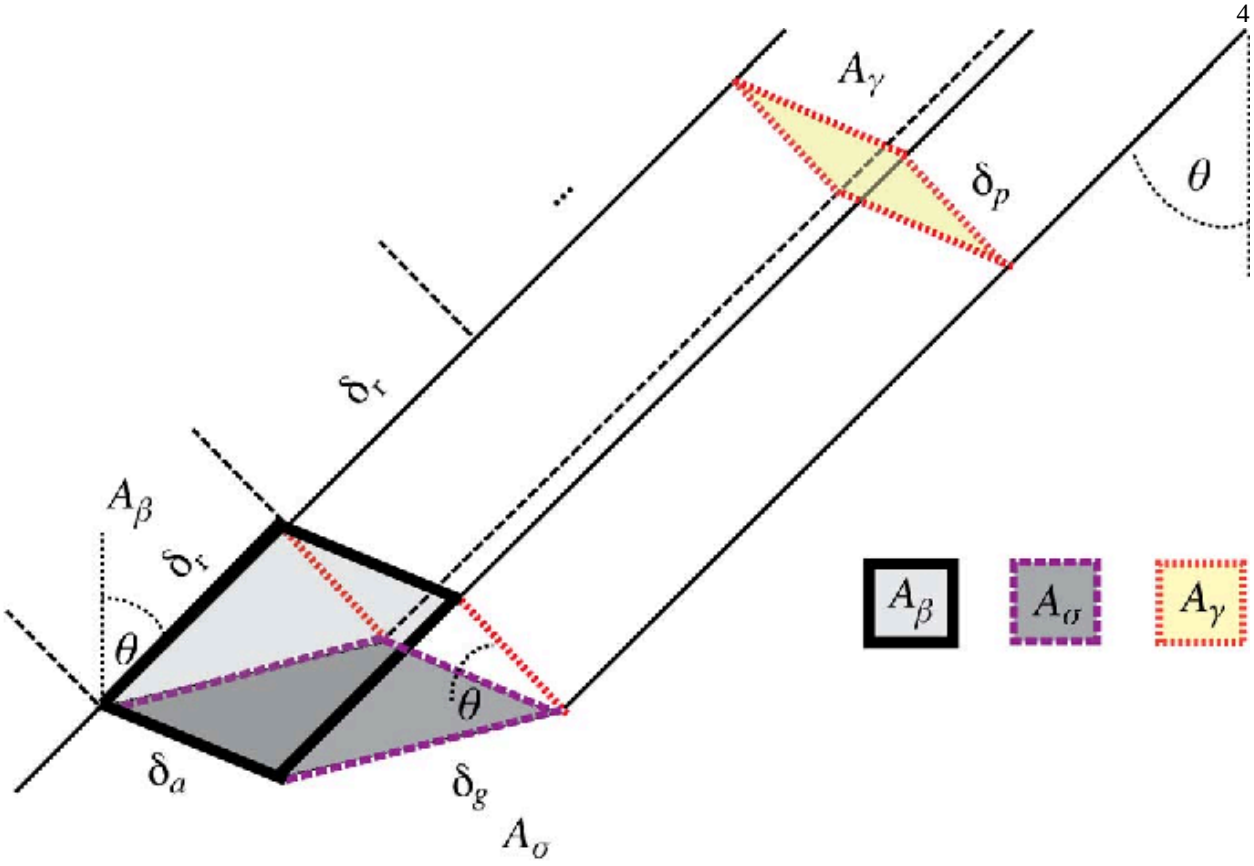

Figure 1. Geometric Conventions for SAR processing. Here the rectangle marked in solid outline is the slant-range plane, the dashed purple area is the ground area (locally tangent to the ellipsoid model of the surface), and the dashed red area is perpendicular to the line of sight from the sensor. From (Small 2011).

1.2 Recent Radar Studies

In addition to biomass estimation using SAR (Sinha et al. 2015), studies have begun using the effects of moisture on backscattering to quantify vegetation and soil moisture (Moghaddam and Saatchi 1999, Hornacek et al. 2012, Steele-Dunne et al. 2012, Brancato et al. 2017), and canopy fuel load (Andersen, Hans-Erik; McGaughey Robert; Reutebuch, Stephen; Schreuder, Gerard; Agee, James; Mercer 2003, Saatchi et al. 2007, Tanase et al. 2015). Recently the direct effect of plant surface moisture on the received radar backscatter has been experimentally measured in a controlled environment (Brancato et al. 2017). Using an anechoic chamber, the study found that increasing plant surface moisture decreases the interferometric coherence, which may result in incorrect measurements of soil moisture or biomass measurements using radar.

Most studies measuring forest biomass operate in the L and P bands, since these bands penetrate the canopy and are scattered mainly by trunk and stem features (Dobson et al. 1992, Ranson and Sun 1992, Wang et al. 1995, Mitchard et al. 2009, Nizalapur et al. 2010, Robinson et al. 2013, Sinha et al. 2015). C-band has been shown to not be as sensitive to changes in forest biomass (Wang et al. 1995, Kasischke et al. 1997, Saatchi and Moghaddam 2000), although it has been effective in agricultural crop biomass estimation (Moreau and Le Toan 2003, Steele-Dunne et al. 2017). (Dobson et al. 1991) found that precipitation can have an effect on canopy backscatter in grasses, although this effect is decreased as biomass is increased. The same study found that biomass effects on backscatter saturate at relatively low levels in the C-band, which has been found in additional studies as well (Dobson et al. 1995, Moreau and Le Toan 2003).

The complex dielectric component of a reflecting surface (typically denoted as ε) has an effect on the backscatter and other radar variables, and consists of two parts: permittivity and conductivity. This has been found to correlate with surface water to varying degrees (Moghaddam and Saatchi 1999, Saatchi et al. 2007, Steele-Dunne et al. 2012, Van Emmerik et al. 2015, Watanabe et al. 2015, Brancato et al. 2017). Changes to the dielectric properties of a target or area can change the backscatter received from that target or area.

Since plant surface water has an effect on the radar backscatter, any biophysical variables measured by radar in foliated areas will be effected by the presence of plant surface moisture. In addition, if the effect is large enough, it should show up as a change in backscatter correlated with rainfall, for a given foliated area. Therefore, the objective of this study is to develop a method of measuring the amount of open water within the forest canopy using remotely sensed data and common climatic variables. I define open water content as the sum of the plant surface and atmospheric water vapor residing inside the forest canopy space.

2 Methods

2.1 Study Site

The study was carried on six sites totaling approximately 41 ha (Figure 2), which are located within the HJ Andrews forest in the Western Cascade Range of Oregon (Table 1). HJ Andrews forest covers roughly 6400 ha of mountainous terrain and contains conifer forests typical of the Pacific Northwest of the North American continent, namely Douglas Fir and western hemlock (Schoonmaker and Mckee 1988). The forest has been a long-term ecological research site since 1980, and was established as an experimental forest in 1948. The sites are centered around the UTM coordinates (565600 E, 4900900 N)(UTM Zone 10N, WGS84, degrees), and describe the three stages in the life of a stand: namely mature, young, and middle-aged stands. Each age class is represented by two separate stands within the group. Additionally, five areas outside of the HJ Andrews were investigated to validate forest based findings. The five areas included a golf course to the south and four recently clear cut areas to the west of the HJA Andrews forest (Figure 2). The golf course will serve as control, since golf courses are generally well irrigated and have little to no geometric effects that could cause differential scattering. The clear cuts serve a similar purpose, but includes the scattering from geometric effects due to the abundance of slash piles left from logging activities.

Table 1. Summary statistics of the study areas

Stand	Area	Age	Number of trees	Total height [m]	Elevation (min-max)
1.	7.1	>100	640	38	878 – 961
2.	6.4	35	2104	23	840 – 881
3.	7.6	65	1204	37	802 – 833
4.	5.0	35	1427	24	886 – 924
5.	10.0	>100	1071	51	837 – 903
6.	4.8	65	799	35	805 – 831

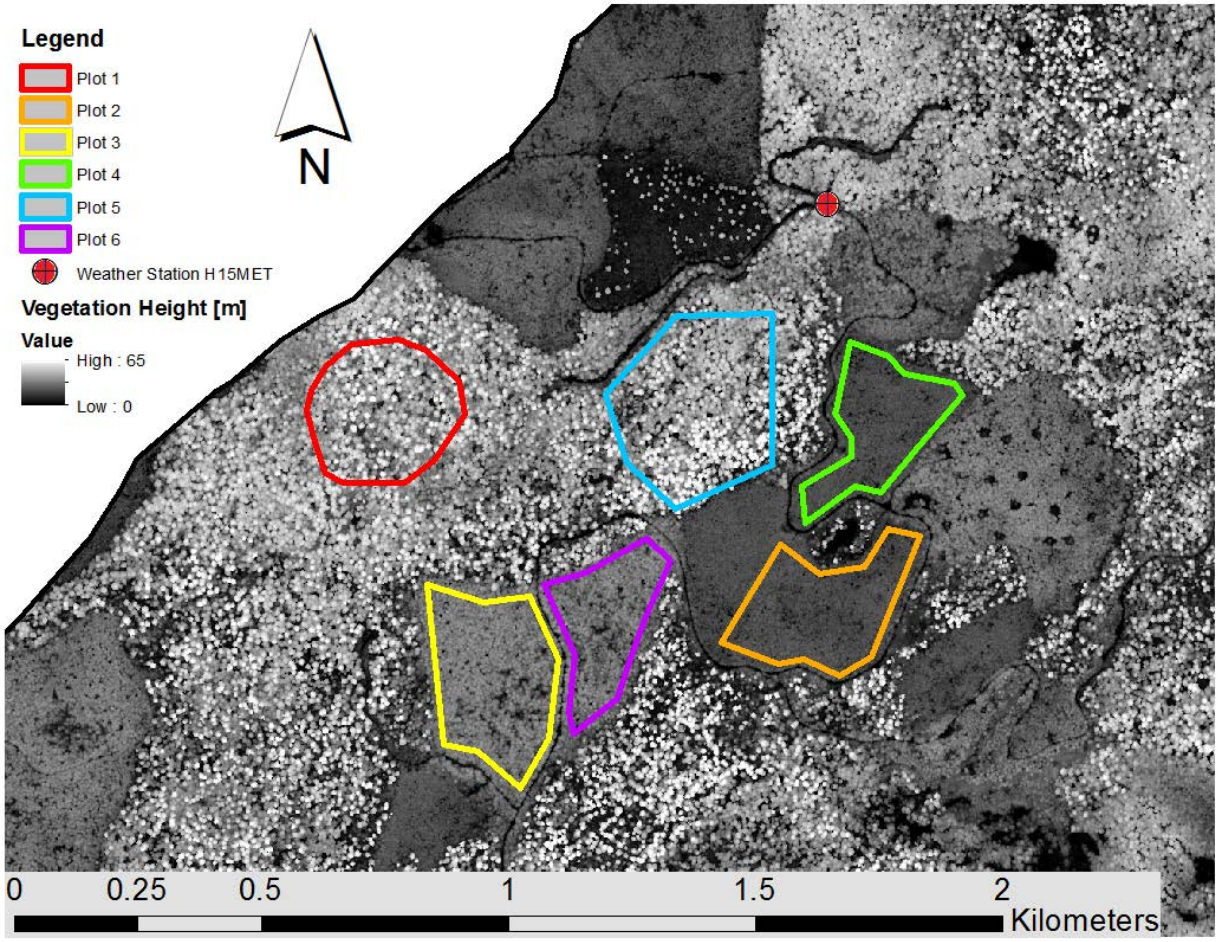

Figure 2. Study areas and the weather station

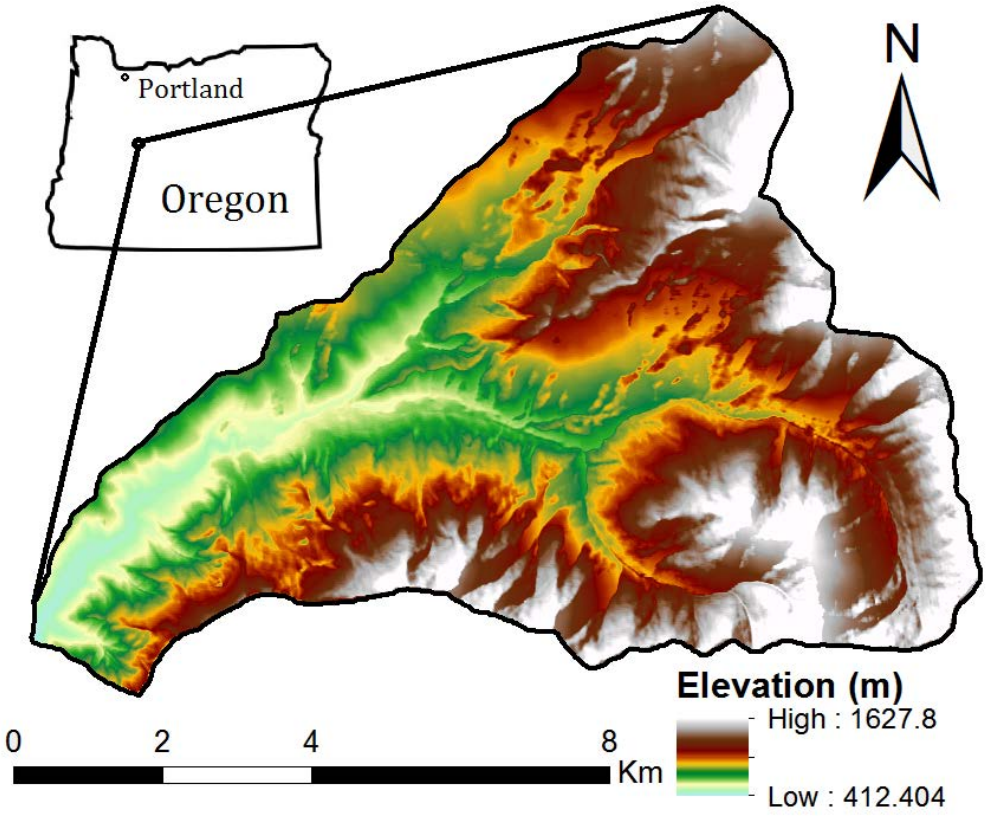

Figure 3. HJ Andrews location in Oregon, USA.

2.2 Input data

2.2.1 Radar Data and Image Processing

To model open water within forest canopy, I have used the radar data provided by Sentinel-1 constellation. Among the SAR satellites, the Sentinel-1 constellation, developed by the European Space Agency, supplies radar images with a high spatial resolution (i.e., approximately 10 m) since 2016. The Sentinel-1 constellation contains two sun-synchronous near-polar satellites: Sentinel-1A and Sentinel-1B. Each satellite has a revisit times of 6 days and 12 days with respect to local time, as ascending passes occur at dusk, while descending passes occur at dawn. The two satellites are equipped with a 12 meter radar array that operates in the C-band (5.405 GHz) with two polarization modes (HH+HV, VV+VH). A thorough overview of the technical aspects of the satellites as well as the data collection process is provided by (Torres et al. 2012). The ease and open access to Sentinel-

1 data, combined with the characteristics of the C-band, make this mission prone to investigation of long-term canopy dynamics at a high spatio-temporal resolution. Several authors had developed landscape level models on water from data supplied by Sentinel-1 (Balzter and Balzter 2001, Hornacek et al. 2012, Joshi et al. 2016).

The Sentinel-1 data were obtained from the ESA portal(2014). Preprocessed imagery was downloaded in ground-range convention (GRDH) for spring to fall dates (April 17 through October 31) during 2015, 2016, and 2017. I excluded all images that contain ice or snow, as frozen water behave differently than liquid water due to differences in dielectric properties (Dobson et al. 1991, Small 2011). To exclude any residual snow or ice I used as minimum temperature 5° Celsius, as I considered that at 5° C all the snow and ice would have melted. I processed the GRDH images with the Sentinel-1 Toolbox (S1TBX), a program that outputs images ready to interpret by addressing all issues, corrections, and calibrations associated with radar imagery, such as thermal noise removal, terrain correction, or de-speckling (Figure 4). During S1TBX processing the radar signal was converted to gamma-naught (γ_0) convention to account for the terrain geometric and radiometric effects (Small 2011).

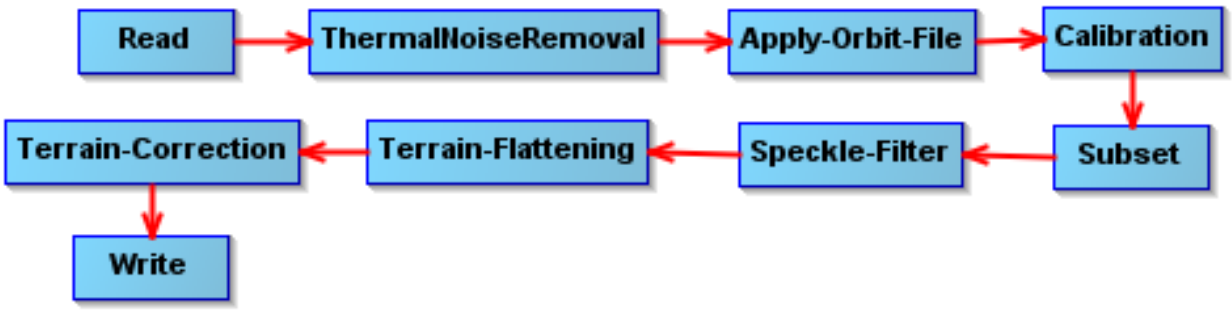

Figure 4 Preprocessing workflow in Sentinel-1 Toolbox

The raw images downloaded from the Copernicus web portal are in slant range geometry (Figure 5a,) which corresponds to the Lagrangian coordinates in relation to the spacecraft and not in relation to a fixed datum. The processing will position the images in Eulerian coordinates (i.e., preset datum), but it is important to note for future users of this system that the raw data will be either 'flipped' along the east/west axis for ascending images or 'flopped' along the north/south axis for descending images (Figure 5c). Essentially, the raw image records backscatter as range increases from left to right, and along the azimuth track from top to bottom. Therefore, descending images appear to be inverted horizontally, as the spacecraft is travelling north to south, but looking east to west and consequently recording westerly locations as further away (i.e. on the right-side of the image). Similarly, on ascending images the spacecraft is moving south to north, therefore, the top of the image will show the southern information and the bottom will display the northern information. Since the spacecraft is looking west to east the near-range will appear on the left-side of the image and the far-range areas will be on the right-side of the image.

The first step implemented in S1TBX removes the thermal noise inherent in radar imagery (Torres et al. 2012). Next, the coregistration process is applied using the orbit file and terrain correcting. The specifications for the orbital tube in which Sentinel-1 is operating are narrower than previous SAR platforms, which lowers the burst miss-synchronization during data uptake (Prats-Iraola et al. 2015). The orbit file contains the precisely measured satellite position and velocity information during acquisition. Although the metadata does contain orbit state vectors, the precise vectors are not available until several weeks after data acquisition, and are automatically downloaded by S1TBX. The data are then radiometrically calibrated by applying (Eq. 5):

$$value_i = \frac{|DN_i|^2}{{A_i}^2} \qquad 5$$

where *DN* is the digital number of a given pixel *i* and *A* is the transform of pixel *i* for σ^0, γ^0, or β^0 radar convention taken from a look-up table. The transform for γ^0 is:

$$A_\gamma = \sqrt{\frac{{A_{dn}}^2 * K}{\tan(\alpha)}} \quad (6)$$

where α is the local incidence angle and K is the calibration constant.

A speckle filter using a Lee Sigma filter (Lee 1983) was used to reduce speckle in the image. The values used for de-speckling (i.e., one look, a sigma value of 0.9, a 7x7 pixel window, and a 3x3 pixel target window) were obtained by trial and error and selected for image clarity and quality, similarly to Foucher and López-Martínez (2009) Since terrain features influence the local incidence angle, the terrain flattening process normalizes backscatter from ellipsoid based σ^0 to terrain flattened γ^0 according to (Small 2011). The terrain is then corrected with the assistance of an existing DEM, such as that from the Shuttle Radar Topography Mission (Farr et al. 2007). The final output of the preprocessing workflow is a raster of the imaged terrain, with each pixel representing the γ^0 at that location (Figure 5b). Each pixel is 10m by 10m with a horizontal accuracy of 0.2 ± 0.24 meters in the slant range and 0.31 ± 1.31 meters in the azimuth range (Schubert et al. 2017). I co-registered the final radar images using a bilinear geometric transformation, implemented in ArcGIS (ESRI 2018).

The data used for analysis contains the γ_0 stacked by recording time (i.e. each pixel represented a point in space with multiple values of γ_0 over time) and the weather data. I compared the radar images from the dry periods (when total rainfall accumulation < 0.5 mm for two weeks preceding radar acquisition) with the images taken at varying degrees of wetness as measured by the weather station. The wetness was expressed as total rainfall accumulation for 15, 30, 45, 60, 90, as well as hourly accumulations from 2 to 12 hours prior to the radar image acquisition.

a. Raw images from Ascending and Descending orbits

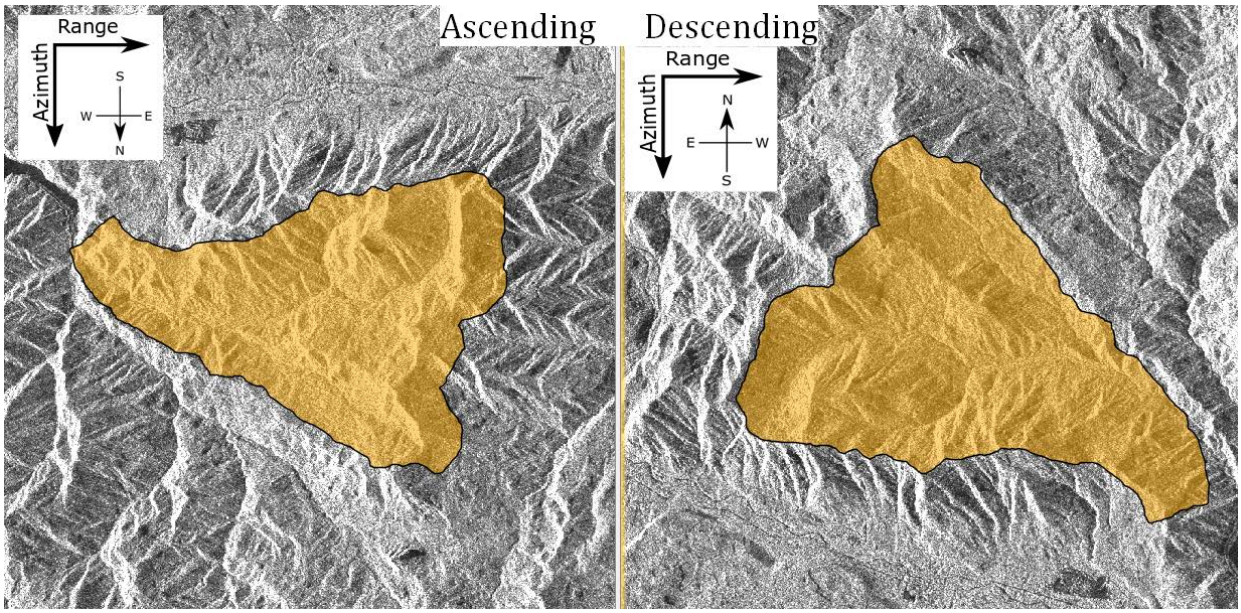

b. Calibrated Image

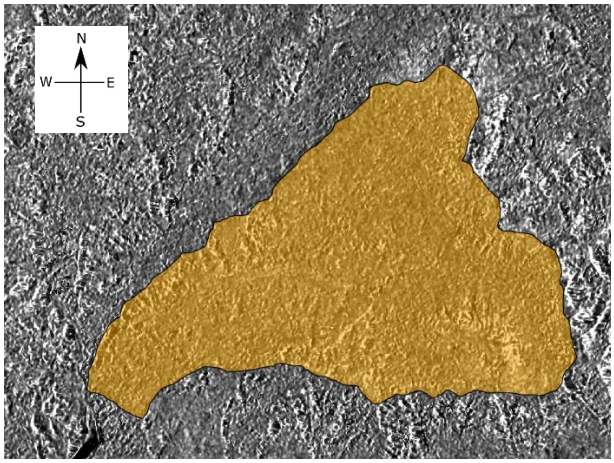

c. Schematic showing Descending data acquisition

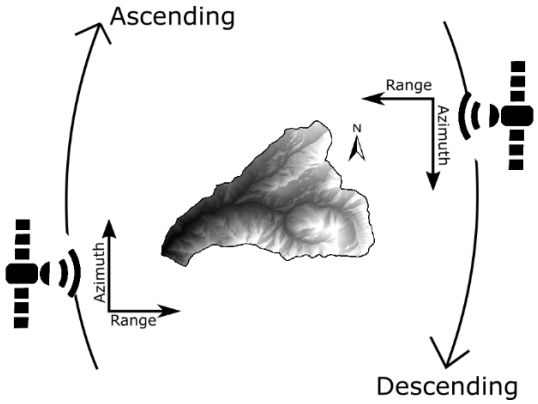

Figure 5. Raw (a) and Processed with S1TBX tools (b) radar images. Note the raw images are geographically inverted due to the data acquisition process shown in (c). The columns of each raw image correspond to increasing range distance from the spacecraft, whereas the rows of each image correspond to the spacecraft movement along its orbital track.

2.2.2 Lidar

The results of Saatchi et al. (2011) suggested that pixel level radar data have limited usage in forestry applications. Therefore, to enhance the information supplied by radar and weather data, I included Lidar , which was obtained from the flights executed in 2016 (Edwards 2018). The system used was a Leica ALS80 mounted on a Cessna Grand Caravan, with an average of 0.89 ground points per square meter. The vertical accuracy of the DOGAMI point clouds is <= 9.25 cm RMSE and the horizontal accuracy is <= 9.25 cm RMSE (QSI 2016). The lidar point clouds were incorporated in the analysis to accurately estimate the size of the trees, such as total height or crown length, which are correlated with the amount of surface water within canopy. Therefore, I hypothesize that tree dimensions would support radar images and weather data in estimation of the water within canopy. I did not explicitly consider the scattering associated with trunk, or branch size and their arrangement, as it has been shown that the needles and moisture of the canopy are responsible for the majority of scatterers in the C-band (Ranson and Sun 1992, Nizalapur et al. 2010, Sinha et al. 2015).

The lidar data includes point clouds, and two derived products, namely the digital surface model (DSM; the 'first hit' comprising the upper surface of the canopy) and the digital terrain model (DTM; the 'ground hits'). I created the Canopy Surface Model (CSM) by subtracting the DTM from DSM. Field measurements revealed that the mean crown length was approximately 50% of the total tree height (N=20, mean = 0.52, variance = 0.016). Based on the ground data I estimated crown length from total tree height as:

$$L_c = 0.52 \times H_{total} \qquad 7$$

where L_C is crown length (in meters), measured from the base of the crown to the top of the tree and H_{total} is the total tree height, in meters.

2.2.3 Weather Data

I obtained the weather data for the study areas from the HJ Andrews data portal (Daly 2016). The weather station used was H15MET, which is roughly 1 kilometer from the study areas (Figure 2). Data is measured in 5 minute (precipitation) and 15 minute (temperature and other atmospheric variables) intervals. Based on the weather data, five

statistics were computed: antecedent moisture condition (AMC), solar radiation, and evapotranspiration, which was estimated with three models. The measures were summed to 15 min, 30 min, 45 min, 60 min, 90 min, and 2, 3, 4, 5, and 6 hours, to match the radar imagery, according to Eq 8.

$$X = \sum_{t=0}^{k} x_i \qquad 8$$

where X is one of the five statistics,

x_i is the value to be summed, which for AMC is the precipitation, and

k is the time, which varies from 15 minutes to 6 hours.

In addition, I computed a variable that estimates how long it had been since rainfall had stopped, defined as < 0.02 mm of rainfall in 30 minutes, henceforth Time Since Rain (TSR). I selected 0.02 mm as the lower threshold considering that the Laplace pressure of a droplet with radius of 0.01 mm is approximately 0.2 atmosphere, value for which the internal pressure of a water droplet still allows shape change in respect with other environmental attributes, particularly temperature.

2.3 Tree identification

Individual tree centroid locations were extracted using TrEX (Strîmbu and Strîmbu 2015). The centroid point of each segmented tree was used to extract information from the radar and topographic rasters (e.g., backscatter, aspect, slope) using an extract-by-points procedure. The trees were placed in tree height classes: large tree (total height > 45 m), medium trees (total height between 30 m and 45 m), and small trees (total height < 30 m). I considered total height in the analysis as it reflects age and size variability, which impacts radar backscatter.

2.4 Evaporation modelling

To model the presence of canopy water, I modelled the effects of rain and evapotranspiration processes of the site using the three different models: Priestly and Taylor (1972), Penman (1948), and Brutsaert (2015), similarly with Ai et al. (2017). I considered the three evaporative models, as they have been shown to approximate wet-canopy evaporation as well as dry evapotranspiration (Klaassen 2001, Ai et al. 2017). The

evaporative loss was subtracted from the accumulated rainfall (AMC) to model canopy water content. Therefore, four SCW values were obtained, one with uncorrected AMC and three that adjust the AMC with the evapotranspiration (Eq. 9):

$$SCW_i = AMC - ET_i \quad (9)$$

where i represents the evapotranspiration model.

2.4.1 Priestley Taylor model

The Priestley-Taylor equation used in this study is:

$$E_{PT} = \alpha_e \frac{\Delta}{\Delta + \gamma}(R_n - G) \quad (10)$$

where E_{PT} is evapotranspiration in mm, α_e is a parameter of the Priestley Taylor equation (unitless), Δ is the rate of change of the saturation specific humidity (unitless), γ is the psychrometric constant [kPa], R_n is net incoming solar radiation [W/m^2] and G is the surface heat flux [W/m^2]. I used a value of 1.05 for the α_e term, as this is the best approximation for this term for coniferous forests (Mcnaughton and Black 1973). To calculate Δ I used the equation from (Murray 1967):

$$\Delta_t = \frac{4098 * \left(0.6108 * e^{\frac{17.27\,T_t}{T_t + 273.3}}\right)}{(T_t + 273.3)^2} \quad (11)$$

where T_t is temperature in degrees Celsius at time *t*. The temperature was measured from the weather station at 5 minute intervals over the course of three years (October 1 2014 to November 21 2017).

The psychrometric constant is estimated by the equation:

$$\gamma = 0.000665 * 101.3 * \left(\frac{293 - 0.0065z}{293}\right)^{5.26} \quad (12)$$

where z is altitude in meters, which varies from 802 to 961 meters within the stands. The overall difference between the lowest and highest elevations results in roughly 0.5 mm difference in the evapotranspiration, and so an approximate mean values of 880 m was used for z.

For net solar radiation, I used:

$$R_n = R_{in} - R_{out} \quad (13)$$

where R_n is the net radiation, R_{in} is incoming radiation, and R_{out} is outgoing (longwave) radiation (Allen et al. 1998). The incoming solar radiation was measured by a nearby weather station (CENMET) and outgoing longwave radiation was calculated using the Stefan-Boltzman law:

$$R_{out} = \sigma\left((T_t + 273.3)^4\left(0.34 - 0.14\sqrt{e_a}\right)\right) \quad (14)$$

where σ is the Stefan-Boltzman constant ($5.67*10^{-8}$ [Wm/K^4]), T_t is the temperature in Celsius at time t, and e_a is the actual vapor pressure [kPa]. Although an additional term for cloud cover is present in the FAO model, I did not have the available cloud cover data and so excluded the effect of clouds on the longwave radiation. The effect of albedo was applied to the incoming solar radiation, using a value of 0.12 for forest cover (Ogunjemiyo et al. 2005) such that

$$R_{in} = R_{measured} * (1 - 0.12) \quad (15)$$

The final term in the Priestley Taylor equation is G, the ground heat flux. This is a simplified version of the model for G in (Bennett et al. 2008), here I are measuring heat flux at the surface, whereas they integrate over the soil layer and through time. For simplicity I used:

$$G = \frac{I * (T_t + 273.3)}{\sqrt{\pi}} \quad (16)$$

where I is the thermal inertia of the bulk soil material

$$I = \sqrt{\rho c k} \quad (17)$$

Where ρ is bulk density, c is specific heat, and k is thermal conductivity (Bennett et al. 2008). I is found to be 0.66 for evergreen coniferous forests according to the findings of (Bennett et al. 2008) and that value is used for this study.

2.4.2 Penman model

I used the Penman equation as outlined in (Penman 1948):

$$E_{pa} = \frac{\Delta}{\Delta + \gamma}(R_n - G) + \frac{\gamma}{\Delta + \gamma}(f_e(u_2))(e_2^* - e_2) \quad (18)$$

where E_{pa} is evapotranspiration in mm, Δ is the slope of the saturation vapor pressure curve, γ is the psychrometric constant, R_n is net radiation, and G is surface ground heat flux, all as calculated above. Additionally I have the terms $f_e(u_2)$, the wind function, and e_2^* and e_2, the saturation vapor pressure and actual vapor pressure, respectively, at 2 meters height above the surface.

The wind function is the same as the simplified function used in (Ai et al. 2017), which was adapted from (Brutsaert and Stricker 1979):

$$f_e(u_2) = 0.35 * (1 + 0.54u_2) \quad 19$$

Where u_2 is the wind speed at a height of 2 meters, which can be calculated using:

$$u_2 = u_z \sqrt[7]{\frac{2}{z}} \quad 20$$

Where u_z is windspeed in [m/s] at height z [m]. The wind detector for this study was at an altitude of 4.5 meters, and although it was not directly located inside the stands under study this calculation was nonetheless included. While most studies use the Penman-Monteith formulation, here I use the original Penman equation since I do not have measurements of the stomatal conductivity.

2.4.3 Brutsaert model

In addition to the two commonly used equations, I used a third nonlinear equation from (Brutsaert 2015) and explored further by (Ai et al. 2017):

$$E = \left(\frac{E_{po}}{E_{pa}}\right)^2 \left(2E_{pa} - E_{po}\right) \quad 21$$

Where E is evapotranspiration, E_{po} is the potential evaporation and E_{pa} is apparent potential evaporation. As in (Ai et al. 2017) I used the Penman equation for E_{pa} and the Priestley Taylor equation for E_{po}. To transform the models from daily to 15-minutely calculation to conform with the weather station data, the E, E_{po}, and E_{pa} values were divided by 96.

2.4.4 AMC, Time Since Rain, and Time Since Dry

In addition to the modelling of evapotranspiration, I also calculated the water contained in the canopy as a rolling sum of the precipitation measurements from the weather station. I used different sizes of moving windows in 15-minute intervals (e.g. 15, 30, 45, 60 minutes) and hourly windows (e.g. 1, 1.5, 2, 3, 4, 5, 6, and 12 hours) and summed the values of precipitation within that window. This resulted in a value that reflected the accumulated rainfall, such that:

$$A_T = \sum_{i=1}^{T} R_i \qquad 22$$

Where A_T is the accumulated rainfall for a time window T, which is one of (15, 30, 45, etc. minutes). R_i is the incrementally measured rainfall, which is measured by the weather station in 5 minute increments. For example, the 1-hour AMC used a moving window of width 12, meaning 12 5-minute intervals were summed (i.e. i = 1…12, then 2…13, 3…14, etc.) for the length of the entire measurement schedule, which as mentioned before ran from 1st October 2014 to 21st November 2017. The total number of 5 min length records used for analysis was 323233 (i.e., approximately 449 days spread from May 1 to Oct 31).

I also calculated time since rain (TSR) and time since dry (TSD). The TSR is the elapsed time since a rain stopped whereas the TSD is the time passed since the rain started (Eq. 3). I computed TSR and TSD using a minimum rainless or dryless period of 30 min and as elementary time interval 5 min, which is the interval for weather recordings.

$$TSR = \sum_{t=0}^{n} (T_{i+1} + T_i)_{accumulated\ rain < threshold} \qquad 23$$

TSR and TSD are defined by the amount of accumulated rainfall. In our study I considered that a threshold to the accumulated rainfall (AMC_T). For TSR, I set a threshold of less than 0.02 mm in 30 minutes (AMC_{30}) as being ‘dry’. I estimated the TSR and TSD using a moving windows approach. Consequently, a simple for-loop proceeds through the weather data frame and checks whether the AMC_{30} value from the beginning to the end of the data reaches the preset threshold. Once the threshold is achieved, a counter begins such that

each successive time step with less than 0.02 mm AMC_{30} would add to this counter, and any AMC_{30} greater than that would reset the counter. Similarly, for TSD, a for-loop checks for values of AMC_{30} greater than 0.02 mm, indicating a 'wet' time-step and adds a counter to the TSD variable. This gave us two additional variables that were informative of the timing of a given radar measurement in relation to rain events.

2.5 Statistical Comparisons

Simple summary statistics were computed for providing an overview of the data used in analysis. The summary statistics were supplemented with plots of various attributes (such as SCW, backscatter, or temperature) against total height and TSR. I initially assessed the changes in the SCW and backscatter against tree height, AMC, and TSR with a simple ANOVA. Based on the findings of Dobson et al. (1992), I assumed that different tree heights would have a different backscatter not only in magnitude but also in variability. Therefore, I compared the variability within the data with an F-test. The comparisons were executed across vegetation height classes in 1, 2, 3, 4, and 5 -meter increments, as well as on the orbital path (ascending or descending).

To test the dependency of SCW on radar backscatter, rain, and tree attributes, I performed a general linear model (GLM) of the form

$$SCW = \gamma + AccT + TSR + S \qquad 24$$

where γ represents the backscatter, AccT is the accumulation time, that is the size of the sliding window (i.e., 15 min, 30 min, etc), TSR is time since rain, and S represents the stand (i.e., a class variable). Since dates with no rain were not pertinent to the modelling of rain, these were dropped prior to forming the GLM to prevent overfitting.

The GLM assumptions of normality and heteroscedasticity, and independence were tested using Shaprio-Wilks test, F-test, and Durbin-Watson test respectively. The differences between the amounts of SCW at different times since the rain stopped was assessed using least-square means and Tukey's multiple comparisons test.

To model the amount of rain water inside the canopy I assumed that the SCW depends on the time elapsed since the rain stopped (TSR), the accumulated water from the rain (AMC), size of the trees (i.e., total height or canopy length), and the radar backscatter (γ). Several formulations would be tried aiming at results that supply significant models with reduced variance of the residuals and meet the regression assumptions. Because the model considers time as a predictor, the covariance structure has to be identified. I selected five types of possible covariance structures, which are commonly encountered in environmental investigations: compound symmetry, heterogeneous compound symmetry, variance components, autoregressive of order 1, and unstructured. I selected final selection covariance structure using Akaike Information Criterion (AIC), as recommended by Fitzmaurice et al. (2004). If more than one structure supplies the smallest AIC, I will choose the covariance structure based on the smallest number of parameters defining the covariance. The order of selection will be compound symmetry, autoregressive of order 1, variance components, heterogeneous compound symmetry, and unstructured. To assess the model we will be using four measures, similar to Fang and Strimbu (2017) and ver Hoef and Temesgen (2013), namely bias, mean absolute bias, root mean square error, and pseudo-coefficient of correlation:

$$bias = \frac{\sum_{i=1}^{n}(y-\hat{y})}{n} \qquad 25$$

$$MAB = mean\ absolute\ bias = \frac{\sum_{i=1}^{n}|y-\hat{y}|}{n} \qquad 26$$

$$RMSE = root\ mean\ square\ error = \sqrt{\frac{\sum_{i=1}^{n}(y-\hat{y})^2}{n}} \qquad 27$$

$$R^2 = pseudo\ R^2 = 1 - \frac{\sum_{i=1}^{n}(y-\hat{y})^2}{\sum_{i=1}^{n}(y-\bar{y})^2} \qquad 28$$

To assess the performance of the model we split the six stands in two categories: one for model development (i.e., stands #1, 2, 3) and one for assessment (i.e., stands # 4, 5, 6). I executed the assessment using the same four measures employed in models development: bias, MAB, RMSE, and pseudo R^2. Data manipulation and preparation was executed in R 3.3.3 and ArcGIS 10.4, whereas all the statistical analyses were performed in SAS 9.4.

3 Results

3.1 Backscatter and tree height

Although the stands were comprised of different sizes of trees, they behaved in a similar way in regards to their mean backscatter (Fig 7 - 9 and Table 2). For all stands, the backscatter decreased in brightness overall during rain events (Figure 9), though this decrease still showed a substantial spread in backscatter values (~5 dB). An interesting finding was that stands with larger trees displayed a smaller variation in backscatter, expressed as the interquartile range (Figure 7).

I found significant differences between levels ($p < 0.0001$) for all tree height increment levels (1 – 5 meter intervals). However, low R^2 values were obtained ($R^2 < 0.01$). Similar results (i.e, $p < 0.0001$) were obtained when the vegetation was grouped into the three broad classes (small, medium, and large), as Tukey-Kramer test revealed significant differences between classes. However, the mean backscatter for each height class was within the range of the other two classes, which suggests the possibility that the significance is the result of the sample size rather than the actual difference.

Table 2. Backscatter Summary Statistics

Stand	Number of trees	Vegetation height [m] std.dev/min/max	Backscatter [dB] Mean (min/max)	Backscatter Variance (Kurtosis/Skewness)
1	640	11.5 / 17 / 77	-7.38 (-11.11 / -0.85)	1.222 (0.07 / -0.07)
2	2104	2.7 / 14 / 38	-7.50 (-12.47 / 1.02)	1.402 (0.37 / -0.02)
3	1204	3.4 / 19 / 44	-7.59 (-10.98 / -3.72)	1.134 (-0.16 / -0.01)
4	1427	2.0 / 17 / 30	-7.58 (-11.79 / -3.63)	1.284 (0.20 / -0.01)
5	1071	12.1 / 17 / 77	-7.75 (-11.16 / -3.53)	1.178 (0.08 / 0.13)
6	799	4.6 / 7 / 45	-7.50 (-12.02 / -1.99)	1.233 (0.25 / 0.03)

3.2 GLM Model

I examined TSR of up to three hours in developing the model study, but did not extend TSR further in the model as the backscatter signal plateaued after this time despite

AMC levels. This agrees with the findings of Keim and Link (2018), who found that the mean residence time of intercepted rainfall does not exceed 1 hour. Additionally, the models which were based on purely pixel-level analysis of radar data performed poorly when compared to those using tree- and stand-level data from lidar.

The GLM model $SCW = \gamma + TSR + S$ has an R^2 value of 0.303, the highest of the models tested in this study, and all terms are deemed significant ($p < 0.0001$). All the stands behave similarly in regards to how long it has been since the last rainfall, despite having different canopy heights and depth (Figure 6).

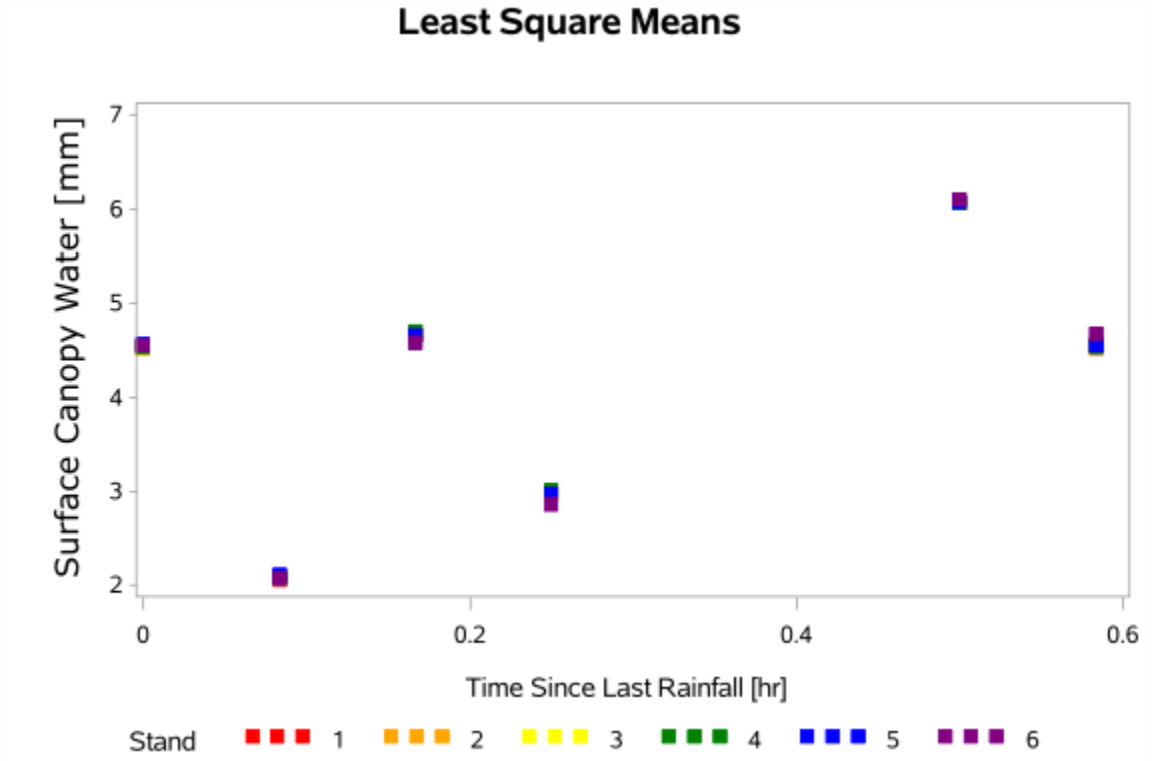

Figure 6. Least Square Mean of SCW plotted against Time Since Last Rainfall.

3.3 Orbital Path

The Levene's Test for homogeneity of variance (HOV) and Welch's test were both run on the orbital path against backscatter (Figure 7). The difference in ascending and descending orbit were significant ($p < 0.0254$). The mean backscatter for ascending orbits was -7.848 dB (standard deviation of 0.957 dB) and for descending orbits was -7.865 dB (standard deviation of 1.115 dB).

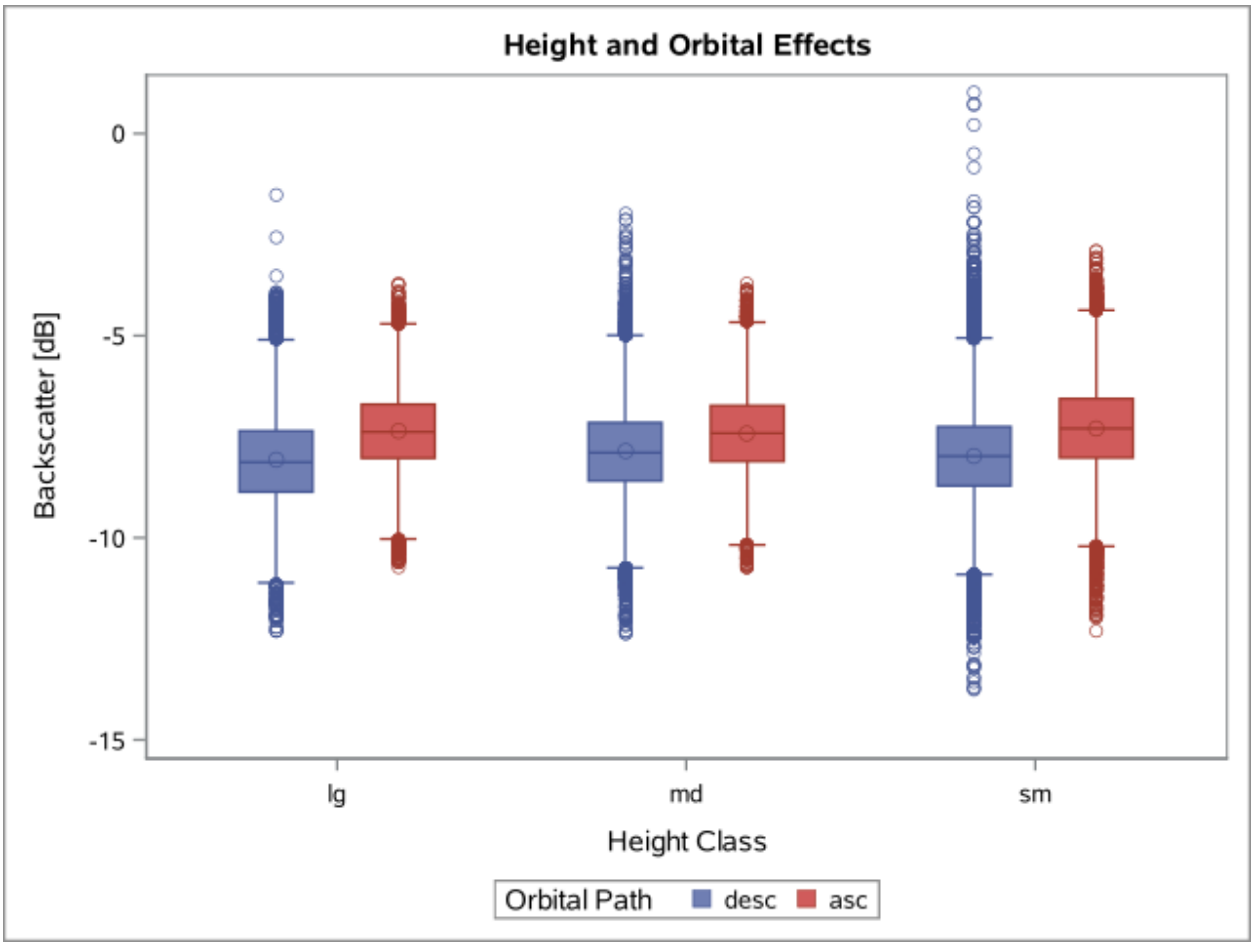

Figure 7. Comparison of Ascending and Descending orbits for three height classes.

The clearing area revealed a significant difference ($p < 0.0001$) between the ascending and descending orbit, showing that dawn and dusk have different backscatter (i.e., for ascending passes is -8.404 dB whereas descending passes has -7.246 dB). The golf course, as expected, displayed a more narrow variation in backscatter, although the mean showed larger degree of variability than the stands in the HJA. The ascending and descending passes exhibited significantly different means (i.e. -15.918 dB and -15.683 dB for the ascending and descending passes, respectively, $p < 0.0002$).

3.4 Temperature

An ANOVA on temperature effects on backscatter showed significant difference in variance ($p < 0.001$), and the R^2 value was 0.228 (Figure 8).

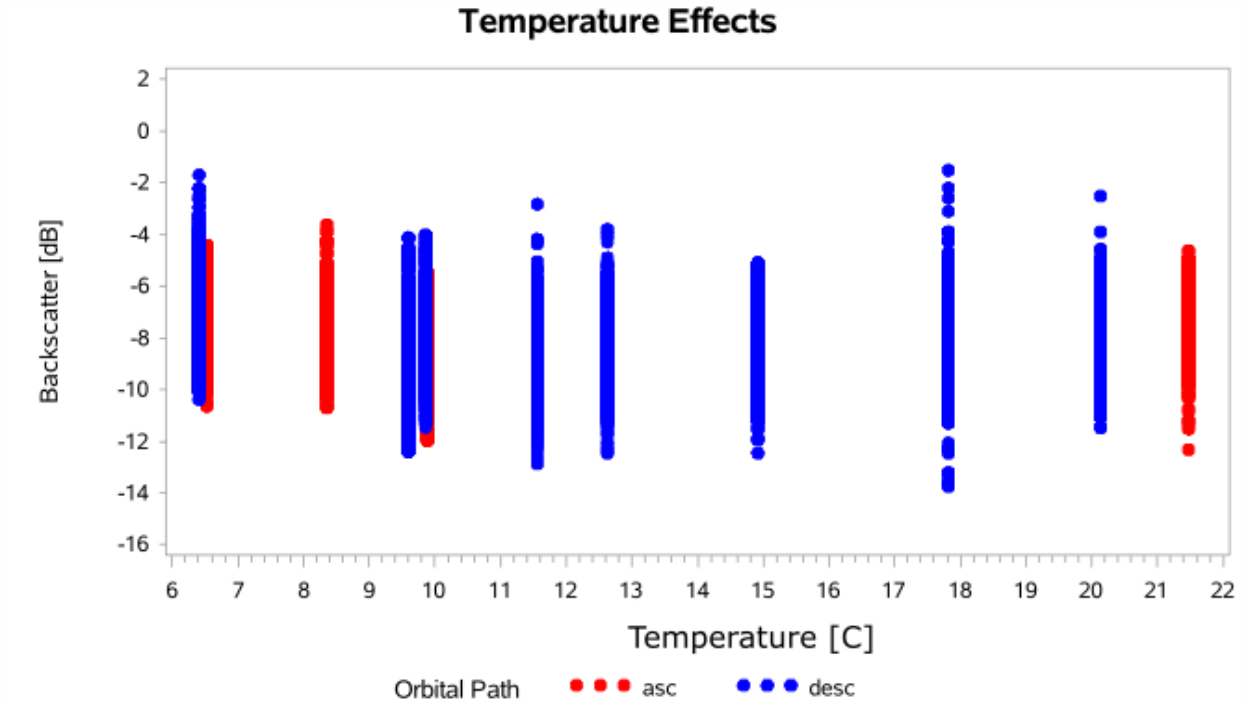

Figure 8. Temperature plotted against backscatter. A slight increase in backscatter brightness is observed at lower temperatures (6-10 C) compared with higher temperatures.

3.5 Water content modelling

The models that used the evaporative scheme (Penman, Priestly-Taylor, and Brutsaert) performed better at predicting than the simplified AMC model. The same GLM discussed above had an R^2 value larger than 0.30 for all models ($p < 0.0001$). However, when using AMC to express SCW, the resulting model had an R^2 value of 0.256, which was still significant ($p < 0.0001$). The three statistics used for comparison of the models supported the significant difference between the evapotranspiration adjusted and unadjusted SCW models ($p < 0.01$). Nevertheless, the SCW computed considering the evapotranspiration were not significantly different among themselves ($p > 0.1$), irrespective bias, MAE, and RMSE. The three models (Penman, Priestly-Taylor, and

Brutsaert) differed by less than 1% in terms of the R^2 value (0.300, 0.303, and 0.303 respectively).

Considering that radio waves are differentially reflected by wet surfaces (Dobson et al. 1995, Watanabe et al. 2015), I tested whether or not the backscatter changes from dry to rainy conditions. I found the backscatter to be significantly different during the rain from dry periods ($p < 0.0001$), but the R^2 was a mere 0.078 (Figure 9 and Figure 10).

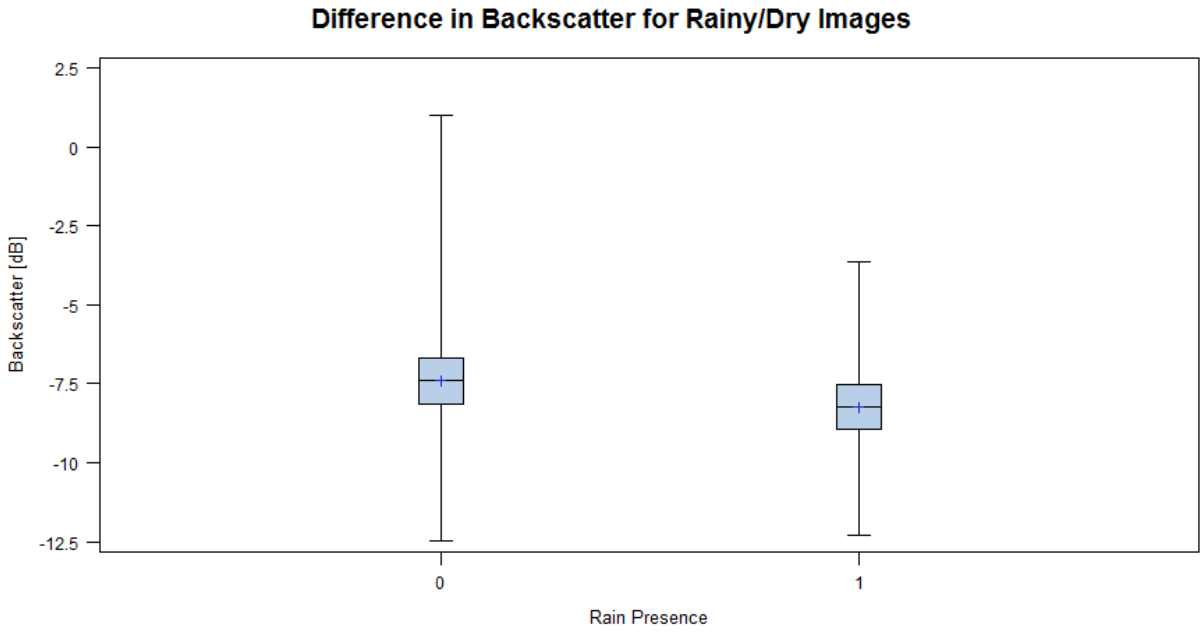

Figure 9. Comparison of backscatter during (1) or not during (0) a rain event. Note, there were only six images during a rain event.

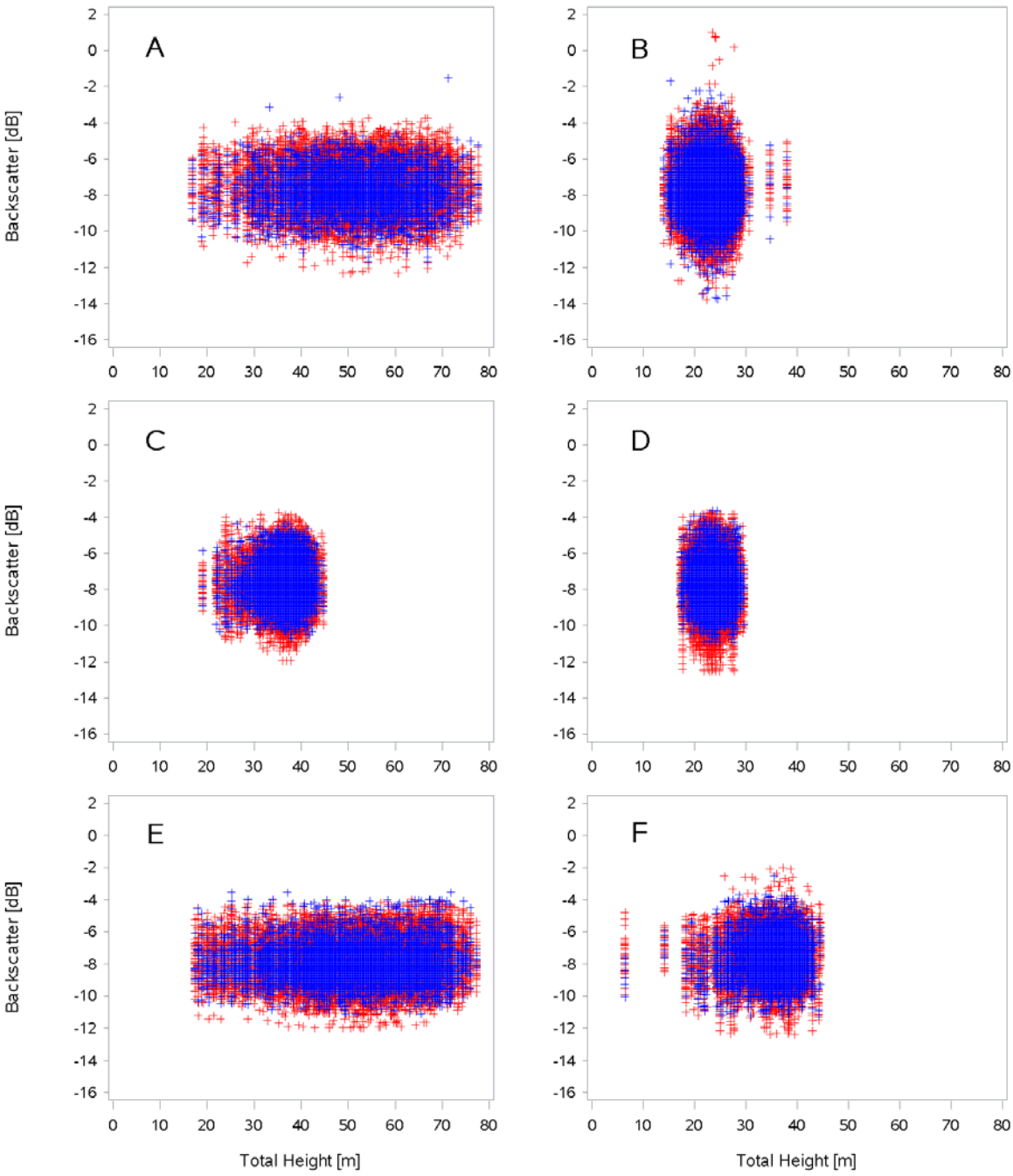

Figure 10. Stand level differences in backscatter between varying heights of trees as well as the presence (blue) or absence (red) of rain during data acquisition. Stands 1-6 are denoted by the letters a-f.

4 Discussion

4.1 General trends

Backscatter appears to be correlated with the presence of rain (i.e. when the image is taken during a rain event) as expected, but a stronger correlation was exhibited between the canopy depth and the time of day when the image was acquired (as per the orbital state). Following the envisioned trend, the backscatter from the clearcut areas displays an even greater degree of variability than the vegetated stands. The increase in variability associated with clearcuts is most likely due to the lack of vegetation cover and abundance of woody debris, which create a surface dominated by complex scatterers and negligible attenuation.

The larger spread in backscatter values for smaller trees than in larger trees, could be caused by the greater canopy attenuation of the radar pulse by the deeper canopies (i.e., taller trees). Shorter trees cause less attenuation and therefore some ground effects may be present in the signals. Another possible cause of an increase backscatter of smaller trees compared with larger trees may be related to greater distance to the ground in the taller trees, enabling more scattering and attenuation before reaching the ground.

4.2 Orbital path and day-time acquisition

The orbital path at acquisition (either descending or ascending) plays a critical part in the overall backscatter of the image. Although all images are corrected for terrain effects, there is not a generalized calibration for diurnal environmental effects such as dew. The ascending passes, taken during local dusk, have higher backscatter overall. Although this effect is statistically significant it is not large enough to produce a practically significant change (Figure 7). Compared to local dusk during the summertime, local dawn in the Pacific Northwest typically has a lower temperature and more dew present, which could account for the decrease in backscatter. After correcting for dates with no prior rainfall the difference between ascending and descending images is reduced further.

4.3 Temperature

Although the temperature did not heavily influence the backscatter directly, its effects on the physical processes governing water storage and uptake may have led to the increase in radar brightness at lower temperatures. Although sub-freezing and near-freezing temperatures were excluded, the effects on water droplet shape and canopy storage capacity with temperature (Klamerus-Iwan and Błońska 2018) must surely be a factor in the reflectivity of water to C-band microwaves.

4.4 AMC and evapotranspiration adjusted AMC

The SCW adjusted with the three-evapotranspiration models performed significantly better than simply the AMC, which suggests that the simple additive form of SCW lacks predictability. The large difference in model predictability indicates that simplified approaches for modelling estimated SCW is less accurate than the approaches that consider evaporative loss, which are inherently complex. This should not come as a surprise, but such a large disparity in the two approaches to moisture modelling suggests that evaporative loss is crucial in estimating the effect of precipitation on the C-band radar backscatter.

As shown by the difference between the two approaches to precipitation modelling, the timing of rain events is important to the effect on radar imagery. I found that after about 1 hour after a rainfall ends, the change in backscatter is negligible, though within that time there can be differences (Figure 11). Our findings suggests that the summers of the Pacific Northwest, which are typically dry, will produce radar images relatively insensitive to rainfall. I should point that the results are based on a relatively reduced dataset, as for the three summers (April to October 2016-2018) considered only six dates out of a total of 67 satellite passes had occurred during rain events; three in the morning and three in the evening.

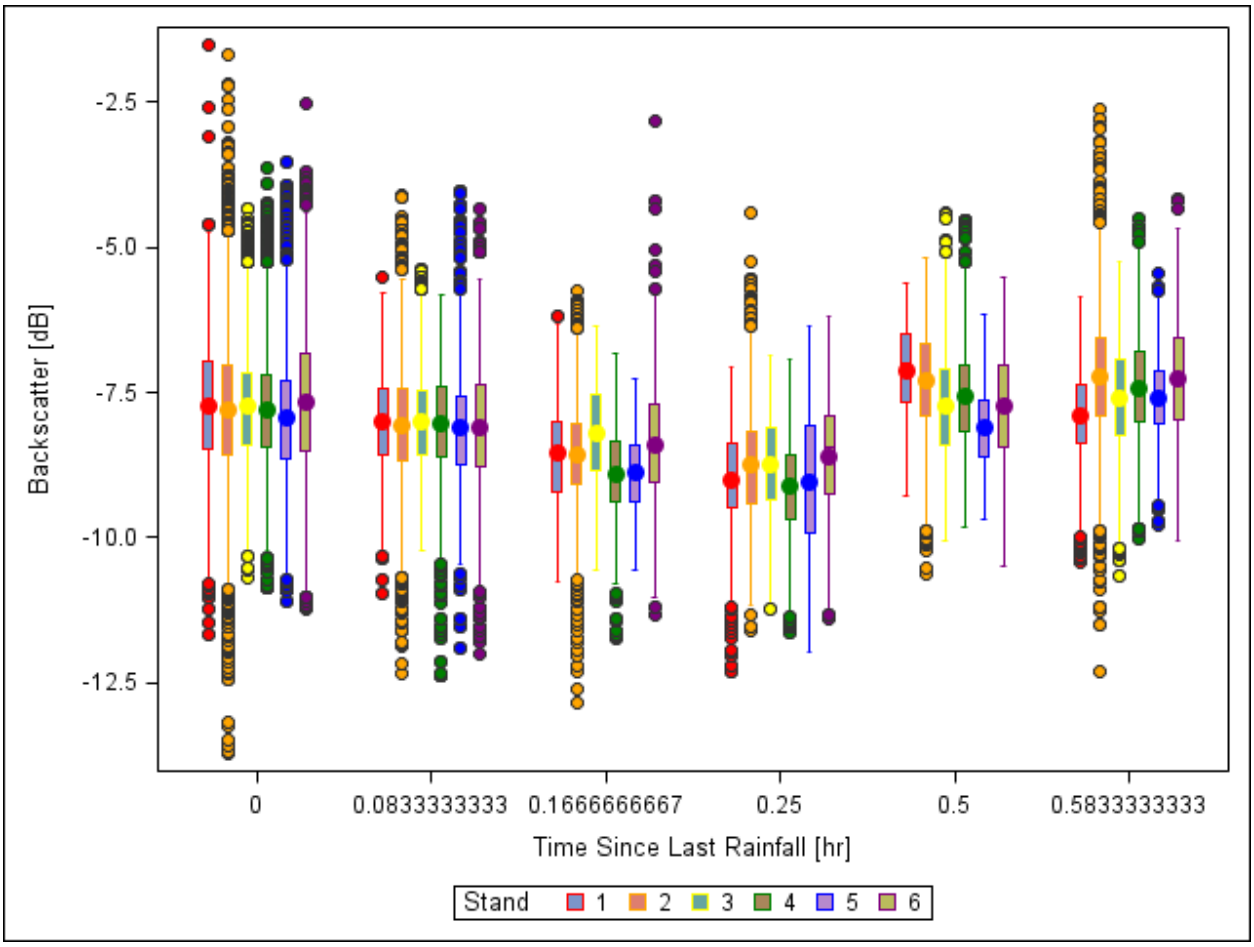

Figure 11. Change in backscatter within 1 hour of rain (TSR < 1hr). A gradual decrease in backscatter occurs up to ~15 minutes, after which the backscatter increases.

Our study provides evidence that SCW can be modeled using radar imagery. To develop a robust and defendable model more data are needed, but the GLM indicates that identification of a formal relationship between SCW, radar imagery and other relatively easy to measure attributes of freely available data is possible. Another finding of this study is that SCW should be modelled using values relevant to the investigation as elementary units, namely the tree and not the pixel. Our results mirror the previous studies which had difficulties in developing a relationship between water content and other variables using pixels. I were able to find evidence of a relationship when I changed the perspective of the investigation, from pixel to tree. This change in perspective was possible because of the inclusion of canopy lidar models, which proved to be crucial in modeling SCW.

It is also important to note that the insensitivity to long-term residual SCW proves to be a bonus in biomass modelling and estimation using C-band in the PNW. One of the major unknown variables in remote radar biomass modelling is typically the water content and its effects on the dielectric component of the model (Karam et al. 1992, Saatchi 1997, Van Emmerik et al. 2015). While biomass does not change drastically over the course of a summer in PNW forests, the available moisture can differ greatly from one hour to the next, particularly at dawn and dusk. Here I have shown that during summer months the dielectric variability of the forests may be a negligible factor when estimating biomass from microwave remote sensing in the C-band.

5 Conclusion

Our study provides evidence that C-band radar is sensitive to summertime tree canopy moisture in the Pacific Northwest forests, but only during or within at most an hour of rain events. Due to the lack of available summer time rain events corresponding to radar acquisition I were not able to develop a predictive model for the effect of rain presence and amount on backscatter or the inverse model of predicting surface moisture amount from a change in backscatter. However, I were successful in revealing a significant relationship between tree canopy length, which is correlated to tree height and age, and the radiometric spreading of the received backscatter. I were able to reach this result because I changed the unit of analysis from pixel to tree. Therefore, I suggest that further studies using radar imagery should use a combination of radar with lidar-derived products (such as projected tree crown).

This study is the first of its kind in the Pacific Northwest, and can serve as the basis of an array of projects in radar remote sensing. To begin with, this study explicitly avoided wintertime observations due to the aforementioned issues with water-ice and wet-snow backscatter. Further investigation in the Pacific Northwest forests should expand the space-time components of this study, beginning with an inquiry into the wintertime behavior of canopy backscatter as well as examining summertime backscatter beyond the HJ Andrews forest. The climatological duality of the Pacific Northwest, both temporally (very wet winters and dry summers) and spatially (coastal, valley, and cascade regions),

means that results from one area or season may not be applicable to another area or season.

6 Bibliography

Ai, Z., Wang, Q., Yang, Y., Manevski, K., Zhao, X., and Eer, D. 2017. Estimation of land-surface evaporation at four forest sites across Japan with the new nonlinear complementary method. Sci. Rep. **7**(1): 1–8. Springer US. doi:10.1038/s41598-017-17473-0.

Allen, R.G., Pereira, L.S., Raes, D., Smith, M., and W, a B. 1998. Crop evapotranspiration - Guidelines for computing crop water requirements - FAO Irrigation and drainage paper 56. Irrig. Drain.: 1–15. doi:10.1016/j.eja.2010.12.001.

Andersen, Hans-Erik; McGaughey Robert; Reutebuch, Stephen; Schreuder, Gerard; Agee, James; Mercer, B. 2003. Estimating canopy fuel parameters in a Pacific Northwest conifer forest using multifrequency polarimetric IFSAR. ISPRS Comm.

Balzter, H., and Balzter, H. 2001. Forest mapping and monitoring with interferometric synthetic aperture radar (InSAR). Prog. Phys. Geogr. **25**(2): 159–177. doi:10.1191/030913301666986397.

Bennett, W.B., Wang, J., and Bras, R.L. 2008. Estimation of Global Ground Heat Flux. J. Hydrometeorol. **9**(4): 744–759. doi:10.1175/2008JHM940.1.

Brancato, V., Liebisch, F., and Hajnsek, I. 2017. Impact of Plant Surface Moisture on Differential Interferometric Observables: A Controlled Electromagnetic Experiment. IEEE Trans. Geosci. Remote Sens. **55**(7): 3949–3964. doi:10.1109/TGRS.2017.2684814.

Brutsaert, W. 2015. A generalized complementary principle with physical constraints for land-surface evaporation. Water Resour. Res.: 1353–1358. doi:10.1002/2014WR016559.Received.

Brutsaert, W., and Stricker, H. 1979. An advection - aridity approach to estimate actual regional evapotranspiration. Water Resour. Res. **15**(2): 443–450. doi:10.1029/WR015i002p00443.

Daly, C. 2016. METEOROLOGICAL DATA FROM BENCHMARK STATIONS AT THE ANDREWS

EXPERIMENTAL FOREST, 1957 TO PRESENT. Available from https://andrewsforest.oregonstate.edu/data/streaming/provisional-data-portal [accessed 17 April 2017].

Dobson, M.C., Pierce, L.E., McDonald, K., and Sharik, T. 1991. Seasonal change in radar backscatter from mixed conifer and hardwood frorests in northern Michigan. Int. Geosci. Remote Sens. Symp.: 1121–1124. doi:10.1109/IGARSS.1991.579268.

Dobson, M.C., Sharik, T.L., Pierce, L.E., Bergen, K.M., Kellndorfer, J., Kendra, J.R., Li, E., Lin, Y.C., Nashashibi, A., Sarabandi, K., and Siqueira, P. 1995. Estimation of Forest Biophysical Characteristics in Northern Michigan with SIR-C/X-SAR. IEEE Trans. Geosci. Remote Sens. **33**(4): 877–895. doi:10.1109/36.406674.

Dobson, M.C., Ulaby, F.T., LeToan, T., Beaudoin, A., Kasischke, E.S., and Christensen, N. 1992. Dependence of radar backscatter on coniferous forest biomass. IEEE Trans. Geosci. Remote Sens. **30**(2): 412–415. doi:10.1109/36.134090.

Edwards, J. 2018. State of Oregon Department of Geology and Mineral Industries. Available from http://www.oregongeology.org/lidar/ [accessed 25 January 2017].

Van Emmerik, T., Steele-Dunne, S.C., Judge, J., and Van De Giesen, N. 2015. Impact of Diurnal Variation in Vegetation Water Content on Radar Backscatter from Maize During Water Stress. IEEE Trans. Geosci. Remote Sens. **53**(7): 3855–3869. doi:10.1109/TGRS.2014.2386142.

Fang, R., and Strimbu, B.M. 2017. Stem measurements and taper modeling using photogrammetric point clouds. Remote Sens. **9**(7): 1–21. doi:10.3390/rs9070716.

Farr, T., Rosen, P., Caro, E., Crippen, R., Duren, R., Hensley, S., Kobrick, M., Paller, M., Rodriguez, E., Roth, L., Seal, D., Shaffer, S., Shimada, J., Umland, J., Werner, M., Oskin, M., Burbank, D., and Alsdorf, D. 2007. The shuttle radar topography mission. Rev. Geophys. **45**(2005): 1–33. doi:10.1029/2005RG000183.1.INTRODUCTION.

Foucher, S., and López-martínez, C. 2009. an Evaluation of Polsar Speckle Filters. : 845–848.

Hornacek, M., Wagner, W., Sabel, D., Truong, H.-L., Snoeij, P., Hahmann, T., Diedrich, E., and Doubkova, M. 2012. Potential for High Resolution Systematic Global Surface Soil Moisture Retrieval via Change Detection Using Sentinel-1. IEEE J. Sel. Top. Appl. Earth Obs. Remote Sens. **5**(4): 1303–1311. doi:10.1109/JSTARS.2012.2190136.

Joshi, N., Baumann, M., Ehammer, A., Fensholt, R., Grogan, K., Hostert, P., Jepsen, M.R., Kuemmerle, T., Meyfroidt, P., Mitchard, E.T.A., Reiche, J., Ryan, C.M., and Waske, B. 2016. A review of the application of optical and radar remote sensing data fusion to land use mapping and monitoring. Remote Sens. **8**(1): 1–23. doi:10.3390/rs8010070.

Karam, M.A., Fung, A.K., Lang, R.H., and Chauhan, N.S. 1992. Microwave Scattering Model for Layered Vegetation. IEEE Trans. Geosci. Remote Sens. **30**(4): 767–784. doi:10.1109/36.158872.

Kasischke, E.S., Melack, J.M., and Dobson, M.C. 1997. The use of imaging radars for ecological applications - A review. Remote Sens. Environ. **59**(2): 141–156. doi:10.1016/S0034-4257(96)00148-4.

Keim, R.F., and Link, T.E. 2018. Linked spatial variability of throughfall amount and intensity during rainfall in a coniferous forest. Agric. For. Meteorol. **248**(September 2017): 15–21. Elsevier. doi:10.1016/j.agrformet.2017.09.006.

Klaassen, W. 2001. Evaporation from rain-wetted forest in relation to canopy wetness, canopy cover, and net radiation. Water Resour. Res. **37**(12): 3227–3236.

Klamerus-Iwan, A., and Błońska, E. 2018. Canopy storage capacity and wettability of leaves and needles: The effect of water temperature changes. J. Hydrol. **559**: 534–540. doi:10.1016/j.jhydrol.2018.02.032.

Lee, J. Sen. 1983. Digital image smoothing and the sigma filter. Comput. Vision, Graph. Image Process. **24**(2): 255–269. doi:10.1016/0734-189X(83)90047-6.

Mcnaughton, K.G., and Black, T.A. 1973. A Study of Evapotranspiration from a Douglas Fir forest Using Energy Balance approach. Water Resour. Res. **9**(6): 1579–1590.

Mitchard, E.T.A., Saatchi, S.S., Woodhouse, I.H., Nangendo, G., Ribeiro, N.S., Williams, M., Ryan, C.M., Lewis, S.L., Feldpausch, T.R., and Meir, P. 2009. Using satellite radar backscatter to predict above-ground woody biomass: A consistent relationship across four different African landscapes. Geophys. Res. Lett. **36**(23): 1–6. doi:10.1029/2009GL040692.

Moghaddam, M., and Saatchi, S.S. 1999. Monitoring Tree Moisture Using an Estimation Algorithm Applied to SAR Data from BOREAS. **37**(2): 901–916.

Moreau, S., and Le Toan, T. 2003. Biomass quantification of Andean wetland forages using

ERS satellite SAR data for optimizing livestock management. Remote Sens. Environ. **84**(4): 477–492. doi:10.1016/S0034-4257(02)00111-6.

Murray, F.W. 1967. On the Computation of Saturation Vapor Pressure. doi:10.1175/1520-0450(1967)006<0203:OTCOSV>2.0.CO;2.

Nizalapur, V., Jha, C.S., and Madugundu, R. 2010. Estimation of above ground biomass in Indian tropical forested area using multi - frequency DLR-ESAR data. Int. J. Geomatics Geosci. **1**(2): 167–178.

Ogunjemiyo, S., Parker, G., and Roberts, D. 2005. Reflections in bumpy terrain: Implications of canopy surface variations for the radiation balance of vegetation. IEEE Geosci. Remote Sens. Lett. **2**(1): 90–93. doi:10.1109/LGRS.2004.841418.

Penman, H.L. 1948. Natural Evaporation from Open Water, Bare Soil and Grass. Proc. R. Soc. A Math. Phys. Eng. Sci. **193**(1032): 120–145. doi:10.1098/rspa.1948.0037.

Prats-Iraola, P., Rodriguez-Cassola, M., De Zan, F., Scheiber, R., Lopez-Dekker, P., Barat, I., and Geudtner, D. 2015. Role of the Orbital Tube in Interferometric Spaceborne SAR Missions. IEEE Geosci. Remote Sens. Lett. **12**(7): 1486–1490. doi:10.1109/LGRS.2015.2409885.

Priestly, C.H.B., and Taylor, J. 1972. On the Assessment of Surface Heat Flux and Evaporation Using Large-Scale Parameters.

Ranson, K.J., and Sun, G. 1992. Mapping biomass for a northern forest ecosystem using multi-frequency SAR data. Int. Geosci. Remote Sens. Symp. **2**(2): 1220–1222. doi:10.1109/IGARSS.1992.578397.

De Ridder, K. 2001. Rain water storage on plant canopies. J. Geophys. Res. **106**: 819–825.

Robinson, C., Saatchi, S., Neumann, M., and Gillespie, T. 2013. Impacts of spatial variability on aboveground biomass estimation from l-band radar in a temperate forest. Remote Sens. **5**(3): 1001–1023. doi:10.3390/rs5031001.

Saatchi, S., Halligan, K., Despain, D.G., and Crabtree, R.L. 2007. Estimation of forest fuel load from radar remote sensing. IEEE Trans. Geosci. Remote Sens. **45**(6): 1726–1740. doi:10.1109/TGRS.2006.887002.

Saatchi, S., Marlier, M., Chazdon, R.L., Clark, D.B., and Russell, A.E. 2011. Impact of spatial variability of tropical forest structure on radar estimation of aboveground biomass.

Remote Sens. Environ. **115**(11): 2836–2849. Elsevier Inc. doi:10.1016/j.rse.2010.07.015.

Saatchi, S.S. 1997. Coherent effects in microwave backscattering models for forest canopies. IEEE Trans. Geosci. Remote Sens. **35**(4): 1032–1044. doi:10.1109/36.602545.

Saatchi, S.S., and Moghaddam, M. 2000. Estimation of crown and stem water content and biomass of boreal forest using polarimetric SAR imagery. IEEE Trans. Geosci. Remote Sens. **38**(2): 697–709. doi:10.1109/36.841999.

Schoonmaker, P., and Mckee, A. 1988. Species Composition and Diversity During Secondary Succession of Coniferous Forests in the Western Cascade Mountains of Oregon. For. Sci. **34**(4): 960–979. doi:10.1093/forestscience/34.4.960.

Schubert, A., Miranda, N., Geudtner, D., and Small, D. 2017. Sentinel-1A/B combined product geolocation accuracy. Remote Sens. **9**(6): 1–16. doi:10.3390/rs9060607.

Sinha, S., Jeganathan, C., Sharma, L.K., and Nathawat, M.S. 2015. A review of radar remote sensing for biomass estimation. Int. J. Environ. Sci. Technol. **12**(5): 1779–1792. doi:10.1007/s13762-015-0750-0.

Small, D. 2011. Flattening gamma: Radiometric terrain correction for SAR imagery. IEEE Trans. Geosci. Remote Sens. **49**(8): 3081–3093. doi:10.1109/TGRS.2011.2120616.

Spatial, Q. 2016. 2016 McKenzie River.

Steele-Dunne, S.C., Friesen, J., and Van De Giesen, N. 2012. Using diurnal variation in backscatter to detect vegetation water stress. IEEE Trans. Geosci. Remote Sens. **50**(7 PART1): 2618–2629. doi:10.1109/TGRS.2012.2194156.

Steele-Dunne, S.C., McNairn, H., Monsivais-Huertero, A., Judge, J., Liu, P.W., and Papathanassiou, K. 2017. Radar Remote Sensing of Agricultural Canopies: A Review. IEEE J. Sel. Top. Appl. Earth Obs. Remote Sens.: 1–25. doi:10.1109/JSTARS.2016.2639043.

Strîmbu, V.F., and Strîmbu, B.M. 2015. A graph-based segmentation algorithm for tree crown extraction using airborne LiDAR data. ISPRS J. Photogramm. Remote Sens. **104**: 30–43. doi:10.1016/j.isprsjprs.2015.01.018.

Tanase, M.A., Panciera, R., Lowell, K., and Aponte, C. 2015. Monitoring live fuel moisture in semiarid environments using L-band radar data. Int. J. Wildl. Fire **24**(4): 560–572.

doi:10.1071/WF14149.

Le Toan, T., Beaudoin, A., Riom, J., and Guyon, D. 1992. Relating Forest Biomass to SAR Data. IEEE Trans. Geosci. Remote Sens. **30**(2): 403–411. doi:10.1109/36.134089.

Torres, R., Snoeij, P., Geudtner, D., Bibby, D., Davidson, M., Attema, E., Potin, P., Rommen, B. ??rn, Floury, N., Brown, M., Traver, I.N., Deghaye, P., Duesmann, B., Rosich, B., Miranda, N., Bruno, C., L'Abbate, M., Croci, R., Pietropaolo, A., Huchler, M., and Rostan, F. 2012. GMES Sentinel-1 mission. Remote Sens. Environ. **120**: 9–24. Elsevier Inc. doi:10.1016/j.rse.2011.05.028.

Wang, Y., Davis, F.W., and Melack, J.M. 1995. The effects of changes in forest biomass on radar backscatter from tree canopies. Int. J. Remote Sens. **16**(3): 503–513.

Watanabe, M., Motohka, T., Shiraishi, T., Thapa, R.B., Yonezawa, C., Nakamura, K., and Shimada, M. 2015. Multitemporal Fluctuations in L-Band Backscatter From a Japanese Forest. IEEE Trans. Geosci. Remote Sens. **53**(11): 5799–5813. doi:10.1109/TGRS.2015.2415832.

Van Zyl, J.J. 1993. The effect of topography on radar scattering from vegetated areas. IEEE Trans. Geosci. Remote Sens. **31**(1): 153–160. doi:10.1109/IGARSS.1992.578363.

7 Appendix

Abbreviations and Variable Names

AMC – **A**ntecedent **M**oisture **C**ondition, in this paper this is taken to mean the cumulative amount of water over a given period of time (e.g. AMC_{30} is the accumulated precipitation over 30 minutes).

ET – **E**vapo**T**ranspiration, the combined effect of evaporation and transpiration that accounts for the loss of AMC over time.

ESA – **E**uropean **S**pace **A**gency

LUT – **L**ook **U**p **T**able, each Sentinel-1 Level-1 products includes in the metadata a look up table with calibration operators specific to that image.

PNW – **P**acific **N**orth**W**est, the region of North America comprising Northern California, Oregon, Washington, and British Colombia. This region is typified by thick evergreen forests and high annual rainfall

SAR – **S**ynthetic **A**perture **R**adar, a form of radar that uses either 1) the motion of a sensor over time, or 2) radar images taken at different times to produce a radar image of finer spatial resolution than traditional beam-scanning radar. SAR is commonly used in most modern radar sensors.

SCW – **S**urface **C**anopy **W**ater, how much water is contained within the canopy on the surface (as opposed to water contained within the biological structure of the canopy components)

SNAP – **S**e**N**tinel **A**pplication **P**latform, a computer program for processing ESA Sentinel mission images

TSD – **T**ime **S**ince **D**ry, a variable that indicates how long it has been since a rain event began (defined as < 0.02 mm rainfall in 30 minutes)

TSR – **T**ime **S**ince **R**ain, a variable that indicates how long it has been since a rain event ended (defined as > 0.02 mm rainfall in 30 minutes)

VH – **V**ertical **H**orizontal polarization, one of several polarization modes used in radar imaging. This means vertically polarized microwaves are sent out through the antenna and only horizontally polarized backscatter is measured

VV – **V**ertical **V**ertical polarization, this means vertically polarized signals are sent by the antennae, and vertically polarized backscatter is measured.